

## Complex Metallic Alloys

Guido Kreiner, Horst Borrmann, Ulrich Burkhardt, Wilder Carrillo-Cabrera, Christian Kudla, Julien Pierre Amelie Makongo, Yurii Prots, and Marek Mihalkovic<sup>1</sup>

### Introduction

The Network [1] of Excellence *Complex Metallic Alloys* (NoE CMA) is funded by the European Commission within the 6<sup>th</sup> Framework Programme *Nanosciences-Materials-Processes*. Established in July 2005, it consists of 22 partners in 12 European countries including the *Max Planck Society*. The main objective of the NoE CMA is to form an integrated body dedicated to the intelligent search for new metallic materials and their development towards technological applicability. The collaboration between the NoE CMA partners lead to the creation of a European Centre for Metallic Alloys and Compounds (C-MAC) in September 2008 [1].

CMA are intermetallic compounds, which are characterized by giant unit cells containing up to thousands of atoms or in case of quasicrystals by an infinite number of atoms. Early examples of CMA are known since the beginning of the last century but have been considered as rare and special cases of intermetallic compounds. Recent phase diagram studies using state of the art techniques have shown that CMA occur frequently not only in multinary but also in binary systems. Since the phase diagram studies are tedious, expensive and time consuming, special attention has been paid primarily to Al and Mg based systems [2,3] promising the design of advanced light metal intermetallics.

A large number of CMA exhibit homogeneity ranges up to several atomic percent. Even those CMA with narrow homogeneity ranges have turned out to be non-stoichiometric phases with intrinsic disorder in many cases, which implies that an ordered crystal structure is unstable in the experimental accessible phase field. Put differently, entropic contributions play an important role for phase formation and stabilization at higher temperatures. Structure determination of disordered CMA is in many cases a formidable task. It comprises the investigation of long and short range order as a function of composition and temperature as well as structural defects as function of the history of materials.

At the MPI for Chemical Physics of Solids in Dresden CMA are studied with focus on structure, formation, thermodynamic stability, physical properties, and chemical bonding—see Scientific Report *Paradigm Shift in Interpretation of Intermetallic Compounds by Analysis of Chemical Bonding*. Special emphasis is put on the development of novel catalysts and thermoelectric materials based on CMA. The main objective of our work, described here, is to understand disorder phenomena in CMA and their influence on phase stability.

### $\zeta$ -Mg<sub>64</sub>Pd<sub>17</sub>: Complexity arising from giant unit cells, orientational disorder and planar faults

Phase stabilities are determined experimentally by exploring the temperature-composition parameter space at finite temperatures. This is state-of-the-art, however, phase diagrams containing a large number of CMA within a small temperature-composition range are challenging. An extreme example is the Mg-Pd phase diagram with the following intermediate phases [4-6]:  $\beta$ -Mg<sub>6</sub>Pd,  $\gamma$ -Mg<sub>57</sub>Pd<sub>13</sub>,  $\epsilon$ -Mg<sub>306</sub>Pd<sub>77</sub>,  $\zeta$ -Mg<sub>64</sub>Pd<sub>17</sub>,  $\eta$ -Mg<sub>3</sub>Pd,

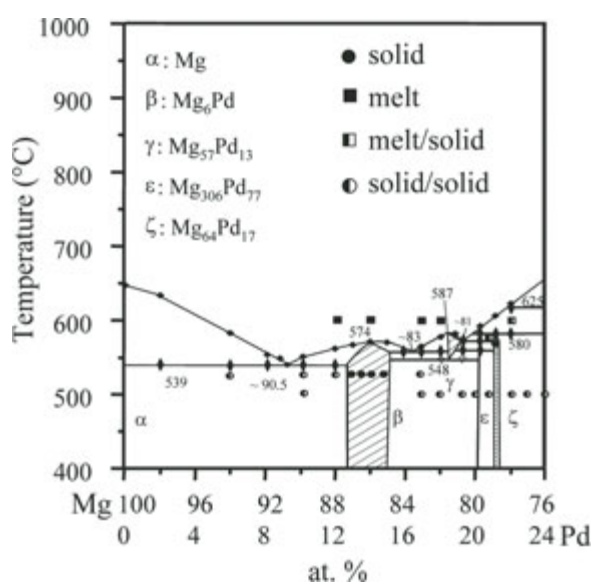


Fig. 1: The Mg-rich part of the Mg-Pd phase diagram [4,5].

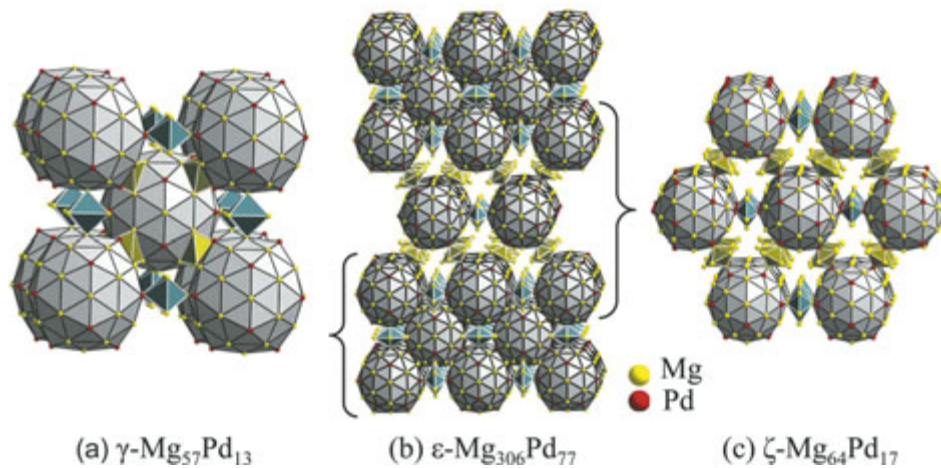


Fig. 2: Crystal structures of Mg-Pd phases close to 80 at.% Mg; (a) bcc packing of MIs in  $\gamma$ -Mg<sub>57</sub>Pd<sub>13</sub> at 81 at.% Mg; (b) intergrowth structure of bcc and hexagonal primitive packed slabs of MIs in  $\epsilon$ -Mg<sub>306</sub>Pd<sub>77</sub> at 80 at.% Mg, and (c) idealized hexagonal primitive packing of MIs in  $\zeta$ -Mg<sub>64</sub>Pd<sub>17</sub> at 79 at.% Mg.

$\theta$ -Mg<sub>5</sub>Pd<sub>2</sub>,  $\iota$ -Mg<sub>2</sub>Pd,  $\kappa$ -MgPd,  $\lambda$ -Mg<sub>0.9</sub>Pd<sub>1.1</sub>,  $\mu$ -Mg<sub>3</sub>Pd<sub>5</sub>,  $\nu$ -MgPd<sub>2</sub>, and  $\xi$ -MgPd<sub>3</sub>. The Mg-rich part of the Mg-Pd phase diagram is shown in Fig. 1. The liquidus curve, the phase fields and heterogeneous equilibria have been determined by analysing several hundred samples of different composition and thermal history.

The phases  $\gamma$ -Mg<sub>57</sub>Pd<sub>13</sub> (*cP*160),  $\epsilon$ -Mg<sub>306</sub>Pd<sub>77</sub> (*oC*1532), and  $\zeta$ -Mg<sub>64</sub>Pd<sub>17</sub> (*oF*1944) form in the narrow composition range from 82 to 79 at.% Mg. They belong to the class of CMAs with Mackay icosahedra (MIs) as fundamental structural units (Fig. 2). The MI has icosahedral symmetry ( $m\bar{3}5$ ) and 55 atoms, here with a composition of Mg<sub>42</sub>Pd<sub>13</sub>. The crystal structure of the  $\gamma$ -phase can be described as a cubic body centred packing of such MIs and the structure of the  $\epsilon$ -phase as an intergrowth of bcc and hexagonal primitive packed slabs of MIs. Therefore, it was expected to find a hexagonal primitive packing of MIs in the crystal structure of the  $\zeta$ -phase with  $a \approx 28.05$  Å and  $c \approx 27.95$  Å as shown in Fig. 2c. Single crystals of the  $\zeta$ -phase could be obtained by the melt centrifugation method close to 79 at.% Mg and 580 °C. X-ray single crystal structure refinement using the hexagonal primitive model in space group *P6/mmm* did not converge to an acceptable *R* factor. A TEM study was carried out [4] since it was not possible to determine the space group symmetry unambiguously from the X-ray data due to pseudo-symmetry and high defect density (see below). A TEM image (Fig. 3a) from the specimen shown in Fig. 3(b) reveals a high density of planar faults by the dark and bright stripes. A HRTEM image (Fig. 3c) par-

allel to  $[001]_H$  shows these planar faults in a higher resolution. The defects are created by three different 120° rotational nano-twin domains.

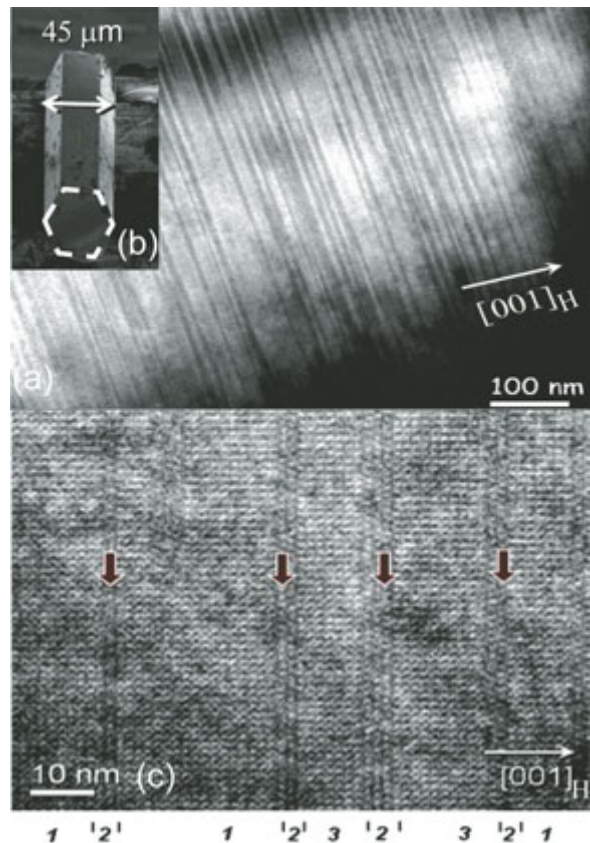


Fig. 3: (a) TEM image of  $\zeta$ -Mg<sub>64</sub>Pd<sub>17</sub> (Philips CM20 microscope) showing planar faults as defects; (b) single crystal of  $\zeta$ -Mg<sub>64</sub>Pd<sub>17</sub> obtained by the melt centrifugation method; (c) HRTEM image (Technai 10) parallel to  $[001]_{H/O}$  showing nano-twinning; the different domains are labeled by numbers at the bottom.

Similar defects could be observed in all specimens obtained by the melt-centrifugation technique as well as in smaller crystals, which were obtained by solidification of the melt and subsequent heat treatment. SAED patterns obtained from Focused Ion Beam (FIB) cuts supplies evidence of an orthorhombic symmetry. As an example a SAED pattern of one isolated domain is shown in Fig. 4a along  $[001]_{\text{H/O}}$ . The pattern has  $mm$  point symmetry, whereas the pattern (Fig. 4b) obtained from thicker slices show the twinned structure. The symmetry of a full set of zones is in agreement with space groups  $Fmmm$ ,  $Fmm2$ , and  $F222$ . The HRTEM image in Fig. 4c obtained from a single domain oriented along the pseudo-hexagonal direction  $[001]_{\text{H/O}}$  zone finally reveals the orthorhombic pseudo-hexagonal packing of Mackay icosahedra. The unit cell parameters obtained from X-ray powder diffraction using an internal standard are  $a = 48.573(6)$  Å,  $b = 28.053(4)$  Å,  $c = 27.986(5)$  Å.

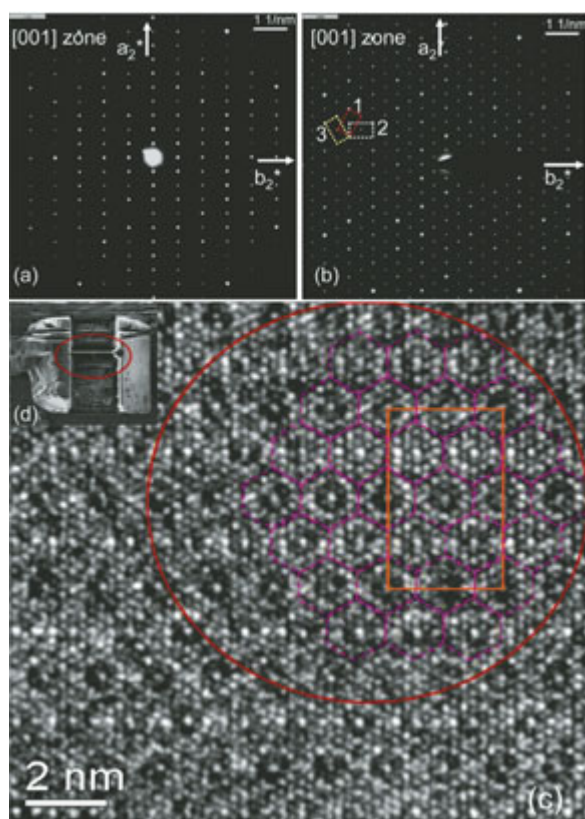


Fig. 4: (a) SAED pattern of one domain of  $\zeta\text{-Mg}_{64}\text{Pd}_{17}$  along  $[001]_{\text{H/O}}$  revealing  $mm$  symmetry; (b) pseudo-hexagonal pattern due to overlapping of  $120^\circ$  rotational twin domains, labelled 1, 2 and 3. (c) HRTEM image of domain 2 revealing a pseudo-hexagonal packing of MIs. (d) FIB cut.

The crystal structure refinement was then carried out with space group symmetry  $Fmmm$ . Starting from the pseudo-hexagonal structural model, the data were refined in such a way to fit the electron density as best as possible and to minimize the  $R$  values. This was possible by introducing mixed occupied sites, partial occupied sites, and some split atom positions. The crystallographic sites were then carefully inspected using criteria like interatomic distances and characteristic site occupations for the Mackay icosahedra as well as for coordination type polyhedra. It was possible to obtain a reliable structural model despite the high density of planar faults.

The crystal structure of the  $\zeta$ -phase can be described as a packing of three crystallographic different distorted rhombic icosidodecahedra (RIs) as shown in Fig. 5a. Two kinds of these shells—in total 75% of the RIs—enclose Mackay icosahedra  $\text{PdMg}_{12}@Mg_{30}\text{Pd}_{12}$  with  $m\bar{3}\bar{5}$  point symmetry. The remaining RIs are filled with  $\text{PdMg}_{12}@Mg_{34}\text{Pd}_{12}$  units with  $6/mmm$  point symmetry displaying in Fig. 5b split atom positions for the inner icosahedron. Two different orientations of  $\text{PdMg}_{12}$ —both with a two-fold axis oriented along  $[001]_{\text{H/O}}$ —have equal probability as shown in Fig. 5c,d.

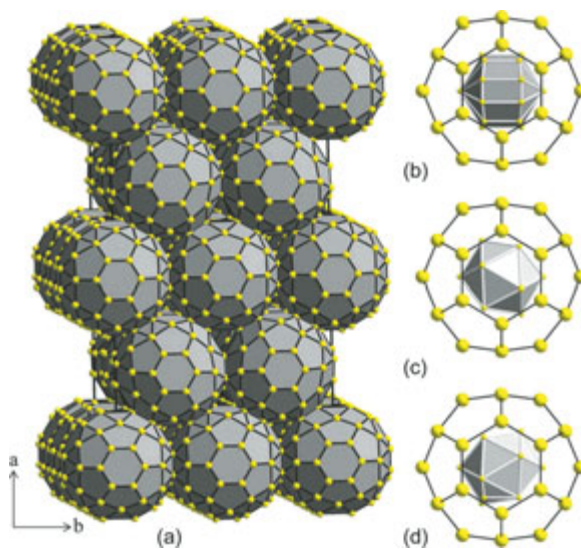


Fig. 5: The crystal structure of orthorhombic  $\zeta\text{-Mg}_{64}\text{Pd}_{17}$ ; (a) packing of distorted rhombic icosidodecahedra (RIs);  $3/4$  of RIs are filled with MIs  $\text{Mg}_{42}\text{Pd}_{13}$ ; (b)  $1/4$  of RIs are filled by  $\text{PdMg}_{12}@Mg_{34}\text{Pd}_{12}$  units displaying split atom positions for the inner icosahedron; (c) and (d) two different orientations of the inner icosahedron  $\text{PdMg}_{12}$ ; two-fold axes of the inner icosahedra are oriented along  $[001]_{\text{H/O}}$ .

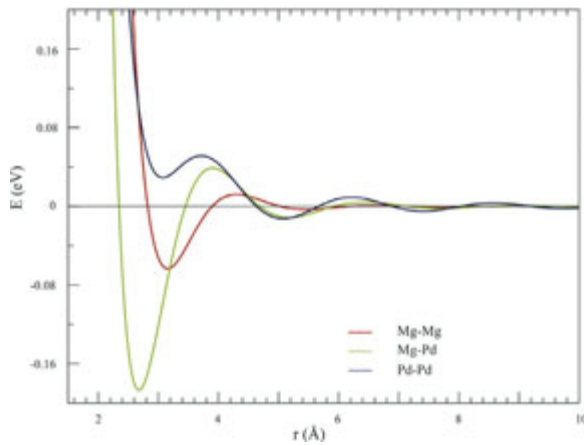


Fig. 6: Pair potentials Pd-Pd, Mg-Pd and Mg-Mg obtained by fitting energies and forces to VASP data of Mg-rich Mg-Pd compounds.

To study the orientational disorder in the  $\zeta$ -phase in more detail, we have performed molecular dynamic calculations (MD) based on pair potentials (Fig. 6). They have been obtained by fitting energy and forces for Mg-rich Mg-Pd compounds against data obtained from first principle calculations using the VASP [7-12] program. In case of nearest neighbor contacts Mg-Pd and Mg-Mg interactions are energetically favored, whereas Pd-Pd contacts are high in energy. Therefore, one can expect that the local structure is governed by Mg-Pd and Mg-Mg interactions. On the other hand Pd-Pd nearest neighbor interactions should be avoided in the structures of Mg-rich compounds, however, they should play an important role in the next nearest shell at about 5 Å.

The results of the molecular dynamic (MD) calculations as shown in Fig. 7 have been obtained by time-averaging atomic trajectories in MD simulations at 800 K and 300 K over 2 and 3 nanoseconds simulation times, respectively. The species in Fig. 7 are not distinguished. The color scale applies to occupation probabilities 0.1-1.0 (red maximal), whereas grayscale applies to the probability interval 0-0.1. The structure of  $\zeta$ -Mg<sub>64</sub>Pd<sub>17</sub> is viewed parallel to the pseudo-hexagonal direction and the thickness of the slice is 7 Å. All atoms except the icosahedron inside the Mg<sub>34</sub>Pd<sub>12</sub> cage vibrate around equilibrium positions, as expected. However, the icosahedron shows continuous features, due to its special degrees of freedom. A 5-

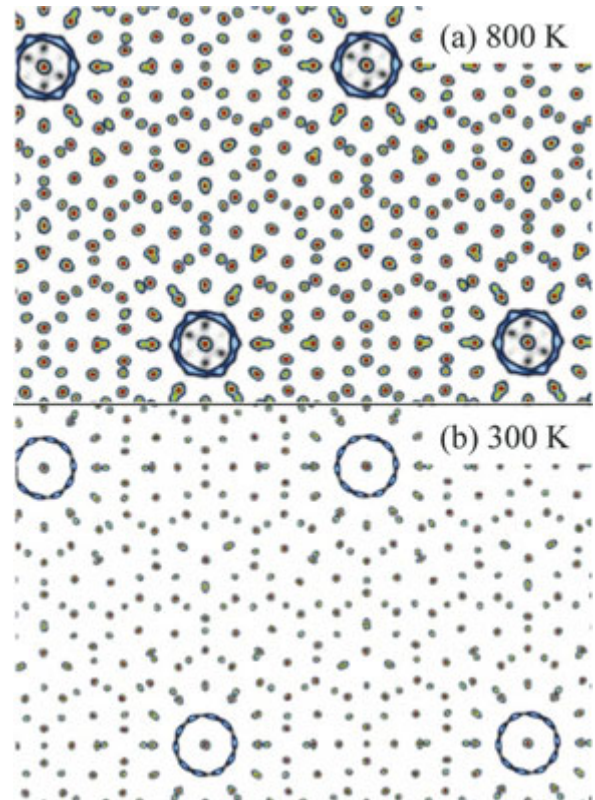


Fig. 7: MD simulations for  $\zeta$ -Mg<sub>64</sub>Pd<sub>17</sub> at (a) 800 K over 2 and (b) 300 K over 3 nanoseconds simulation time; the structure of  $\zeta$ -Mg<sub>64</sub>Pd<sub>17</sub> is viewed parallel to the pseudo-hexagonal axis and the thickness of the slice is 7 Å. The color scale applies to occupation probabilities 0.1-1.0 (red maximal), whereas grayscale applies to the probability interval 0-0.1.

fold axis of the icosahedron aligns with the 6-fold axis of the cage at low temperature. At elevated temperatures, the icosahedron can flip over such that a 2-fold axis is aligned with the 6-fold axis of the cage, as found experimentally. Such a configurational/vibrational degree of freedom of the inner icosahedron is an intriguing phenomenon, peculiar to the intermetallic compounds. Here, it is caused by the fact that Mackay icosahedra in these Mg-rich Mg-Pd alloys form networks, that are eventually non-icosahedral in sense that the point symmetry of the lattice they occupy is not a subgroup of the icosahedral point group, exhibited locally by the Mackay icosahedra. This gives rise to the formation of the hexagonal cage with 6-fold symmetry, accommodating an icosahedron of 12 Mg around a Pd atom.

### Modeling and structure prediction for $\gamma'$ - $\text{Ag}_9\text{Mg}_{37}$

At low temperatures phase diagrams are difficult to investigate because no thermodynamic equilibrium state can be reached within an acceptable time. Here, modelling, i.e., starting from an approximate crystal structure using first principles and pair potential studies has proven to be very helpful to find the ground state structure.

At the same time they provide clues to understand how a particular structure is stabilized. Valuable information can be obtained on the influence of the structural vacancies and substitutional disorder on the phase stability. Quite often this information allows to predict the stability of ternary extensions and therefore to speed up laboratory work. There is even progress in structure prediction of CMAs using simulated annealing techniques. The latter approach still depends on empirical knowledge of the unit cell volume and high quality pair potentials.

The Ag-Mg system [13-18] contains four complex metallic alloy phases:  $\varepsilon$ - $\text{Ag}_7\text{Mg}_{26}$  (cF264),  $\varepsilon'$ - $\text{Ag}_{17}\text{Mg}_{54}$  (oI142),  $\gamma$ - and  $\gamma'$ - $\text{Ag}_9\text{Mg}_{37}$  (hP92). The Mg-rich part of the phase diagram is shown in Fig. 8. The  $\gamma$ -phase forms at 80.3(1) at.% in a peritectoid reaction at 471 °C with no perceptible homogeneity range. The crystal structure as shown in Fig. 9a (space group  $P6_3/m$ ,  $a = 12.4852(8)$  Å,  $c = 14.4117(9)$  Å) can be described as a network of vertex connected and interpenetrating icosahedra.

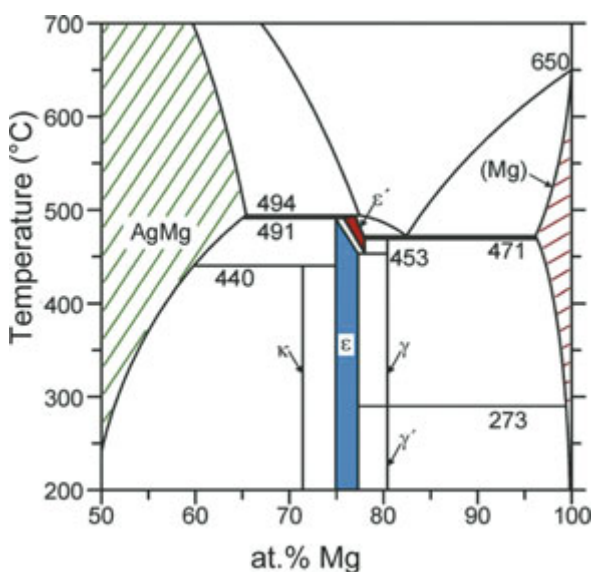


Fig. 8: The Mg-rich part of the Ag-Mg phase diagram [12].

The empty space of this network (grey shaded area in Fig. 9a) is occupied by a chain of CN9, CN12, and CN15 polyhedra. The sequence of polyhedra is random in case of the  $\gamma$ -phase but has a finite correlation length, i.e., there are local rules how to stack the polyhedra.

DSC measurements indicate a phase transition at 273 °C. To predict the crystal structure of the low temperature  $\gamma'$ -phase (space group  $P6_3$ ,  $a = 12.490(1)$  Å,  $c = 14.448(1)$  Å) a simulated annealing approach using pair potentials has been chosen. The pair potentials for Mg-rich Ag-Mg compounds are shown in Fig. 10. The Ag-Mg and Mg-Mg interactions are attractive for nearest neighbor contacts but highly damped beyond the second shell. A striking feature of the Ag-Ag pair potential is its high energy at low distances in combination with a strongly oscillating behavior up to 14 Å. Therefore, the local structure is governed by Ag-Mg and Mg-Mg interactions, whereas the medium range is mainly determined by Ag-Ag interactions.

Simulated annealing was done using an Adaptive Metropolis Monte Carlo Algorithm [19]. The simulation box contained a random mixture of 18 Ag and 74 Mg atoms with dimensions according to the unit cell parameters of  $\gamma'$ - $\text{Ag}_9\text{Mg}_{37}$ . MD runs were carried out for an interval from 430 °C to

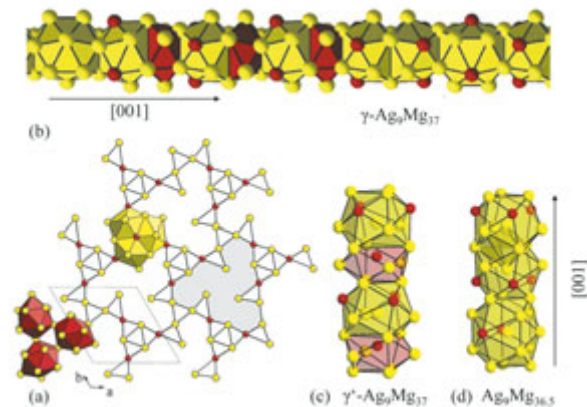


Fig. 9: Crystal structure of high temperature  $\gamma$ - and low temperature  $\gamma'$ - $\text{Ag}_9\text{Mg}_{37}$ ; (a) the backbone of both crystal structures is a network of vertex connected and interpenetrating icosahedra; (b) in case of the  $\gamma$ -phase the remaining space (grey area) is occupied by a polyhedral chain of CN9, CN12, and CN15; here, the sequence is random but has a finite correlation length; (c) in case of  $\gamma'$ -phase the chain is composed of CN9 and CN12 polyhedra commensurate with the periodicity of the backbone; (d) a stacking sequence with CN15, CN12, CN15, CN12 is only slightly higher in energy than that of (c).

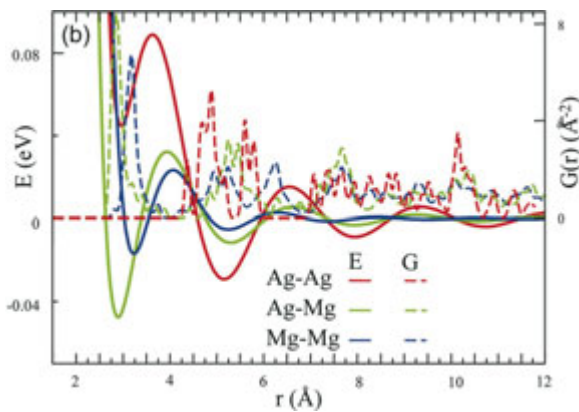


Fig. 10: Pair potentials for Ag-Ag, Ag-Mg and Mg-Mg obtained from VASP data; the partial pair distribution functions of  $\gamma'$ -Ag<sub>9</sub>Mg<sub>37</sub> are overlaid.

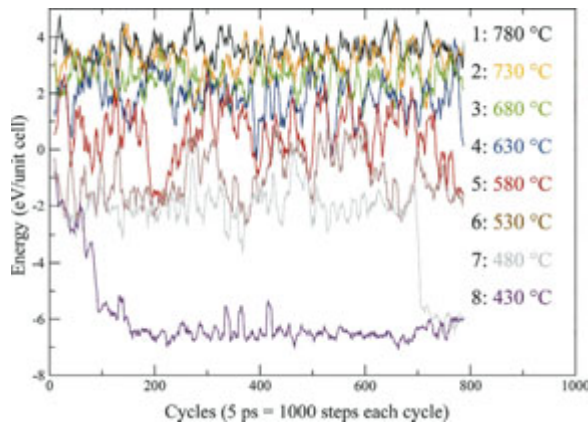


Fig. 11: Simulated annealing using an Adaptive Metropolis Monte Carlo Algorithm. The simulation box contained a mixture 18 Ag and 74 Mg with dimension according the unit cell parameters of  $\gamma'$ -Ag<sub>9</sub>Mg<sub>37</sub>.

780 °C in steps of 50 °C, i.e., enclosing the temperature of the peritectoid formation of  $\gamma$ -Ag<sub>9</sub>Mg<sub>37</sub>. A typical run is shown in Fig. 11. After a small number of cycles an ordered crystal structure appears at low temperature. An amorphous phase and a mixture of  $\beta$ -AgMg and Mg have been obtained by quenching the simulation at 780 °C and 630 °C, respectively. Please note that the formation of  $\gamma$ -Ag<sub>9</sub>Mg<sub>37</sub> is suppressed by using only one unit cell.

The crystal structure is closely related to that of  $\gamma$ -Ag<sub>9</sub>Mg<sub>37</sub>. However, the chain is now composed of CN9 and CN12 polyhedra and is commensurable with the periodicity of the backbone structure. The partial pair distribution functions for this structure are overlaid in Fig. 10. All distances between atoms correlate well with the local minima of the respective pair potentials.

The crystal structure of  $\gamma'$ -Ag<sub>9</sub>Mg<sub>37</sub> is a stable ground state structure according to VASP computations and fits well the experimental powder pattern. The convex hull of the phase diagram is shown in Fig. 12.  $\gamma'$ -Ag<sub>9</sub>Mg<sub>37</sub> is -0.4 meV/atom below the tie line of the neighboring phases Mg and Ag<sub>15</sub>Mg<sub>51</sub>, the latter an ordered variant of  $\epsilon$ -Ag<sub>7</sub>Mg<sub>26</sub>.

To understand the driving force for the phase transition exhaustive computations were done by Metropolis Monte Carlo using pair potentials. In a first step all possible configurations of the CN9, CN12 and the CN15 polyhedra, which fit the local stacking rules of the high temperature phase, were tested. Only two kinds of local rules survived the energy criteria. They are shown in Fig. 9c,d. The alternate stacking of CN9 and CN12 corresponds to the solution found by simulated annealing, i.e., Ag<sub>9</sub>Mg<sub>37</sub> at 80.4 at.% Mg. The other type corresponds to the sequence CN15-CN12-CN12 and has with Ag<sub>9</sub>Mg<sub>36.5</sub> at 80.2 at.% a slightly lower content of Mg. The energy of the structure is only 4 meV/atom above the tie line. It turned out that the energy of all intermediate structures containing both types of local stacking (superstructures) follows a linear behaviour as shown in Fig. 13. By folding back the 2c superstructure of Ag<sub>9</sub>Mg<sub>36.75</sub> at 80.3 at.% onto one unit cell one obtains a similar electron density as found for the disordered high temperature phase (refined composition Ag<sub>9</sub>Mg<sub>36.81(6)</sub>). The stability of the disordered phase can now be explained by configurational entropy contributions. The CN15 polyhedron allows to distribute two silver atoms on three Mg sites of nearly equal energy. In addition superstructures with different correlations, e.g., an or-

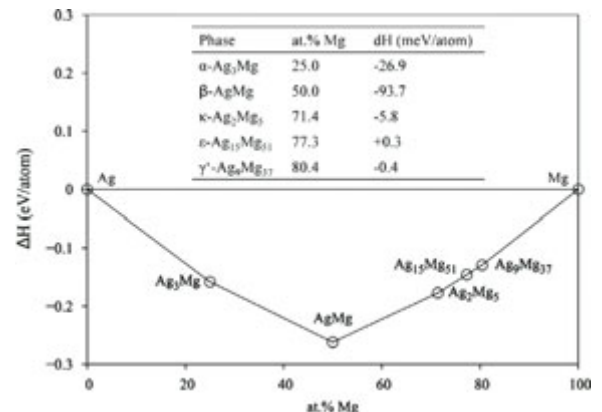


Fig. 12: Convex hull of the Ag-Mg system obtained from VASP data.

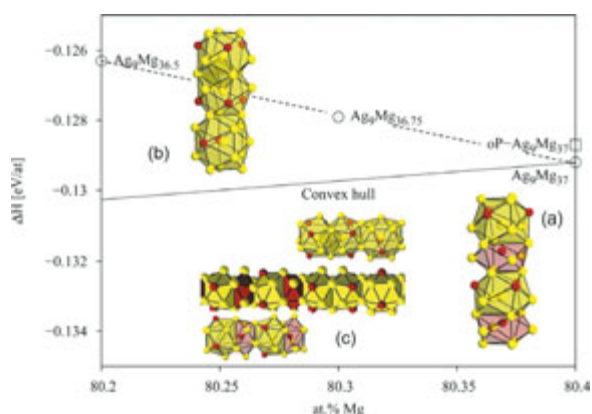


Fig. 13: Part of the convex hull close to  $\gamma'$ - $\text{Ag}_9\text{Mg}_{37}$ . (a) alternate stacking of CN9 and CN12 as found in the ground state structure; close to the tie line is an orthorhombic superstructure; (b) stacking of CN15, CN12 and CN12 in the structure of  $\text{Ag}_9\text{Mg}_{36.5}$ ; the CN15 polyhedron allows configurational disorder by distributing 2 Ag on 3 Mg sites; (c) dashed line corresponds to enthalpy of formation for superstructures containing both stacking sequences; an example at  $\text{Ag}_9\text{Mg}_{36.75}$  is shown as an intergrowth of (a) and (b).

thorhombic primitive superstructure of  $\text{Ag}_9\text{Mg}_{37}$  as shown in Fig. 13, between the polyhedral chains are possible. Due to the very small energy differences between the models from 80.2 to 80.4 at.% Mg—an interval within the error margin of the chemical analysis—one can assume that full equilibrium at low temperature is difficult to obtain. This is in agreement with our observation that good samples of  $\gamma'$ - $\text{Ag}_9\text{Mg}_{37}$  could only be obtained by melt spinning and subsequent long time annealing.

## References

- [1] *CMA Complex Metallic Alloys – European Network of Excellence*: <http://www.cma-ecnoe.org/>
- [2] M. Feuerbacher et al., *Z. Kristallogr.* **222** (2007) 259.
- [3] S. Brühne, E. Uhrig, G. Kreiner, and W. Assmus, *Phil. Mag.* **86** (2006) 463.
- [4] J. P. A. Makongo, *Dissertation*, TU Dresden 2009.
- [5] J. P. A. Makongo, Yu. Prots, U. Burkhardt, R. Niewa, C. Kudla, and G. Kreiner, *Phil. Mag.* **86** (2006) 427.
- [6] C. Wannek, and B. Harbrecht, *J. Solid State Chem.* **159** (2001) 113.
- [7] P. Blochl, *Phys. Rev. B* **50** (1994) 17953.
- [8] G. Kresse, and J. Furthmüller, *Phys. Rev. B* **54** (1996) 11169.
- [9] G. Kresse, and J. Hafner, *Phys. Rev. B* **47** (1993) RC558.
- [10] G. Kresse, and D. Joubert, *Phys. Rev. B* **59** (1999) 1758.
- [11] J. P. Perdew, and Y. Wang, *Phys. Rev. B* **45** (1992) 13244.
- [12] S. H. Vosko, L. Wilk, and M. Nussair, *Can. J. Phys.* **58** (1980).
- [13] C. Kudla, *Dissertation*, TU Dresden 2008.
- [14] C. Kudla, and G. Kreiner, *Z. Kristallogr. (Supplement)* **21** (2004) 170.
- [15] C. Kudla, and G. Kreiner, *Z. Anorg. Allg. Chem.* **630** (2004) 1739.
- [16] C. Kudla, Yu. Prots, A. Leineweber, and G. Kreiner, *Z. Kristallogr.* **220** (2005) 102.
- [17] G. Kreiner, and S. Spiekermann, *Z. Anorg. Allg. Chem.* **627** (2001) 2460.
- [18] A. V. Arakcheeva, O. G. Karpinskii, and W. E. Klesnichenko, *Sov. Phys. Crystallogr.* **33** (1988) 907.
- [19] X. Dong, and E. Blaisten-Barojas, *J. Comput. Theor. Nanosci.* **3** (2006) 118-126.

<sup>1</sup> Academy of Science, Bratislava, Slovakia